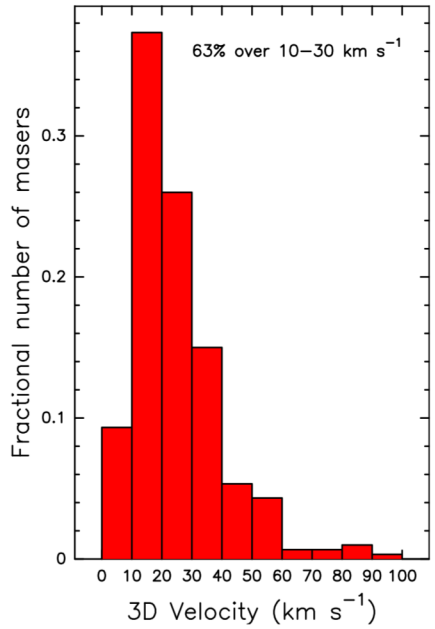

Fig. 3. Histogram of the maser 3D-velocity amplitude, cumulating all the POETS targets. The histogram bin is 10 km s^{-1} and the histogram values are normalized by the total number of masers with measured PMs. The average error on the 3D-velocity amplitude and corresponding standard deviation are 3.3 and 2.5 km s^{-1}.

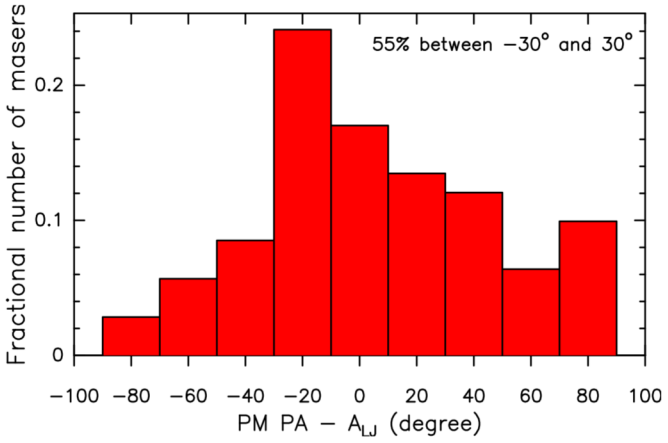

Fig. 4. Histogram of the difference between the maser PM PA and the PA of the jet axis from the literature, A_{LJ}, cumulating all the 14 POETS targets in which a jet has been observed through thermal tracers (see Table A.1 of Paper III). The histogram bin is 20° and the histogram values are normalized by the total number of considered PMs. The target-average error on the PM PA and corresponding standard deviation are 12° and 4°.

the observed water masers move close to the plane of the sky, 92% and 62% within an angle of 35° and 15°, respectively.

3. Discussion

3.1. H_2O masers marking the YSOs

The result presented in Sect. 2.1 is derived from absolute positions (accurate to a few mas) of 994 individual maser cloudlets associated with 36 distinct YSOs (see Table A.1), whose position on the sky and distance are determined with an accuracy of a few 10 mas and 5–10% (via maser trigonometric parallax measurements), respectively. The mas-level accuracy in our VLBI

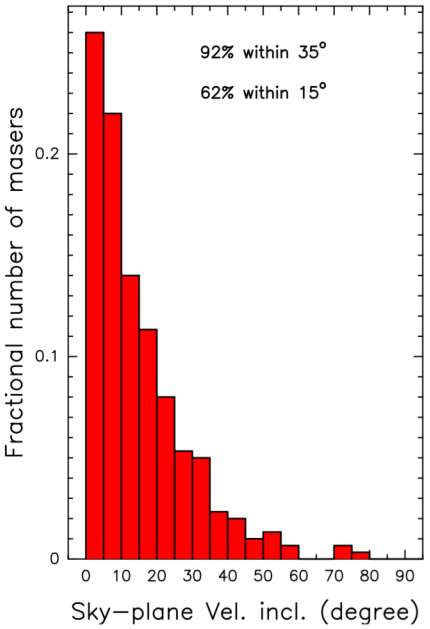

Fig. 5. Histogram of the inclination of the 3D water maser velocity with the plane of the sky, cumulating all the POETS targets. The histogram bin is 5° and the histogram values are normalized by the total number of masers with measured PMs. The average error on the maser velocity inclination and corresponding standard deviation are 7° and 4°.

H_2O maser positions together with the employment of a reliable YSO tracer (i.e., sensitive, rms$\sim$10 μJy beam^{-1}, JVLA A-Array observations) distinguishes ours from previous surveys of interstellar water masers, such as those by Beuther et al. (2002), Walsh et al. (2014), Titmarsh et al. (2016), and Kim et al. (2019). These former surveys were conducted with connected element interferometers (Very Large Array, VLA; Australian Telescope Compact Array, ATCA; Korean VLBI Network, KVN) achieving an angular resolution of $\geq$ 0.″1, which is insufficient for determining the spatial and velocity distribution of individual maser cloudlets.

In these previous surveys, a significant fraction of the water masers is always found to be offset by a few arcsec from the complementary star formation indicators (such as mm-continuum sources and 6.7 GHz CH_3OH masers), calling into question the connection between the water masers and a specific phase of the YSO evolution. This apparent discrepancy can be readily explained by limitations of previous surveys, including poor resolution and sensitivity (typically an order of magnitude worse than POETS for the radio continuum). At 22 GHz, the radio continuum sensitivity of the POETS survey ($\sim$30 μJy over a beam size of 0.″1) allows us to detect the flux from an unresolved, optically thin, HII region excited by a zero-age main-sequence (ZAMS) star with spectral type as late as B5 at a distance of 1 kpc, and B3–B4 at 3–4 kpc. Therefore, sensitive JVLA A-Array continuum observations towards the water masers detected in these previous surveys would provide a critical test of our results by searching for previously undetected cluster components emitting (free–free) radio continuum. Indeed, our results clearly indicate a strong connection between the water masers and an active phase of mass ejection (and accretion) of the YSO.

3.2. The H_2O maser brightness function

We do not find any clear correlation between the intensity of the water maser and its distance from the YSO or its

3D-velocity amplitude. In general, water masers cluster on scales of ∼10 au and it is quite common to find mixed groups of intense and weak masers at similar distance from the YSO. This qualitatively agrees with the shock models for the origin of the H_2O masers, which predict that the peak flux of the masers depends mostly on the LOS velocity coherent, amplification path (Hollenbach et al. 2013, Eq. (14)) in the post-shock gas layers. Then, a large range of maser amplification paths (and intensities) across small regions is naturally expected since: (1) both the density and velocity behind shocks vary on very small scales, namely, ≤1 au (Hollenbach et al. 2013, see Fig. 4); (2) the shock velocities can be inclined at different angles with respect to the LOS; (3) depending on the very local conditions of the ambient medium, shocks can even become fragmented and dissipate. In this way, the scatter in maser intensities owing to the specific shock geometry can conceal a weaker dependence of the maser intensity on the position from the YSO and the shock speed.

The histograms of Fig. 2 indicate that the channel-map detection threshold of ∼100 mJy beam^{-1} of present spectroscopic VLBI measurements is insufficient to adequately image the water maser emission associated with YSOs. In fact, the steep increase of the fractional number of detected masers with decreasing luminosity strongly suggests that there is a multitude of masers with an intensity ≤100 mJy beam^{-1} remaining undetected. In Fig. 2, we report the power-law fits of the histogram values both for the main plot and the inset. We have to consider that the first bins of these histograms are certainly underestimated owing to our limited sensitivity. It should also be noted that the fitted power-law expressions reported in Fig. 2 are not normalized. Requiring that the integral between $0 \leq L_{\rm iso} \leq 30$ Jy kpc^2 be equal to 1, we determine the corrected brightness distribution for weak water masers as:

$$F_{\rm M} = 0.11\ (L_{\rm iso})^{-0.70}. \quad (1)$$

Equation (1) implies that about 50% of the whole water maser population have a luminosity that is less than the typical detection threshold of a few Jy kpc^2 and it is still undetected. The next-generation VLA (ngVLA) will be the appropriate facility to study the spatial and velocity distribution of this large family of weaker masers (Hunter et al. 2018), which can be used to sample the 3D-velocity field around the forming YSO with much better detail. If water masers at a distance of ≲1000 au from the YSOs trace magneto-centrifugal DWs (see Paper III), multi-epoch ngVLA, polarized 22 GHz maser observations can serve as a unique tool to investigate both the velocity and magnetic fields of DWs. Moreover, the ngVLA will permit a simultaneous study of the water masers and the (usually faint) radio continuum of the YSO, improving the precision of the maser positions (and velocities) in the YSO reference frame.

3.3. The origin of H_2O masers in shocks

Concerning the statistics on the properties of the H_2O maser 3D velocities, the first notable result is the global distribution of the PM directions with respect to the orientation of the YSO jet, presented in Fig. 4. The fact that more than half of the observed PMs is oriented on the sky within an angle of 30° from the jet axis implies that, statistically, the observation of only a few maser PMs associated with a given YSO can already suffice to constrain the direction of the protostellar jet. In the literature, there have been several studies published on specific sources assessing that water masers can be reliable tracers of the YSO outflows (see Sect. 1 for references), but our H_2O maser survey first provides a statistic of the water maser PM directions based on a relatively large sample of targets. Figure 4 can also be read that about half of the water masers move along directions forming large angles with the jet. The non-collimated motion, near the YSO, of half of the water masers has been interpreted in Paper III in terms of a wide-angle velocity pattern associated with the outer, less collimated portion of the DW.

The second interesting result is the finding that almost all the measured maser 3D velocities form small angles (≤35°) with the plane of the sky, as indicated by the histogram in Fig. 5. That agrees very well with the shock models for the water masers (Elitzur et al. 1992; Kaufman & Neufeld 1996; Hollenbach et al. 2013), where a long velocity-coherent, amplification path along the LOS is predicted for planar shocks with propagation direction close to the plane of the sky. In this case, there are no large variations of the velocity along the LOS, which permits the formation of intense masers. Therefore, we can explain the histograms in Fig. 5 as an observational bias, given that masers moving at small (large) angles from the plane of the sky have a much higher (lower) detection probability.

In the following, we discuss in more detail the properties of the shocks excited in protostellar winds that can serve as the birthplaces of the H_2O masers. Let us indicate with $V_{\rm w}$ and $\rho_{\rm w}$ the speed and the density, respectively, of the wind, and with $V_{\rm u}$ and $\rho_{\rm u}$ the speed and the density, respectively, of the pre-shock material on which the wind impinges, that is $V_{\rm w} \geq V_{\rm u}$. Both for radiative and adiabatic shocks, the shock velocity, $V_{\rm s}$, approximated by the water maser velocity, can be written as (Masson & Chernin 1993, see Eqs. (3) and (4)):

$$V_{\rm s} \approx V_{\rm u} + \frac{V_{\rm w} - V_{\rm u}}{1 + \sqrt{\rho_{\rm u}/\rho_{\rm w}}}. \quad (2)$$

According to the shock models, H_2O masers originate in post-shock gas layers with (H_2 number) density of $n_{\rm H_2} \sim 10^8$–10^9 cm^{-3} (Hollenbach et al. 2013). These high post-shock densities can be obtained either behind weak C shocks propagating through very dense regions, $\rho_{\rm u} \sim 10^8$–10^9 cm^{-3}, $5 \leq (V_{\rm s} - V_{\rm u}) \leq 40$ km s^{-1}, or behind strong J shocks crossing less dense gas, $\rho_{\rm u} \sim 10^6$–10^7 cm^{-3}, $(V_{\rm s} - V_{\rm u}) \geq 50$ km s^{-1}.

Gas densities as high as 10^8–10^9 cm^{-3} are typical of the few disks discovered around high-mass YSOs (Beuther et al. 2013; Johnston et al. 2015; Ilee et al. 2016; Moscadelli et al. 2019b; Sanna et al. 2019b). DWs are expected to be launched from the surface of such dense disks (Pudritz & Banerjee 2005; Kölligan & Kuiper 2018). On the basis of Eq. (2), weak, internal C shocks in the slower and less collimated regions of DWs, with $\rho_{\rm w} \approx \rho_{\rm u} \sim 10^8$–$10^9$ cm^{-3}, and $10\ {\rm km\ s^{-1}} \leq V_{\rm u} \lesssim V_{\rm w} \leq 40\ {\rm km\ s^{-1}}$, would propagate at speeds of 10–30 km s^{-1}, in good agreement with the peak of the velocity distribution of the water masers shown in Fig. 3. Therefore, based on the analysis of the direction and amplitude of the maser velocities, we suggest that about 50% of the water masers, excited within 1000 au from the YSOs, originate in C shocks internal to DWs.

The highest maser speeds, ≥30 km s^{-1}, of the distribution of Fig. 3 could instead be generated in strong J shocks, which are naturally expected to be associated with fast protostellar jets. The radio continuum emission from thermal jets is thought to be produced in internal shocks and provides a reliable way to estimate the jet properties. At 100–1000 au from the YSOs, typical jet speeds and densities are $V_{\rm w} \approx$ 100–1000 km s^{-1} and $\rho_{\rm w} \sim 10^6$ cm^{-3}, respectively (Anglada et al. 2018; Rosero et al. 2019). If such fast jets impact denser, $\rho_{\rm u} \approx 10^7$–$10^8$ cm^{-3}, stationary, $V_{\rm u} \approx 0$ km s^{-1}, ambient material, Eq. (2) predicts velocities

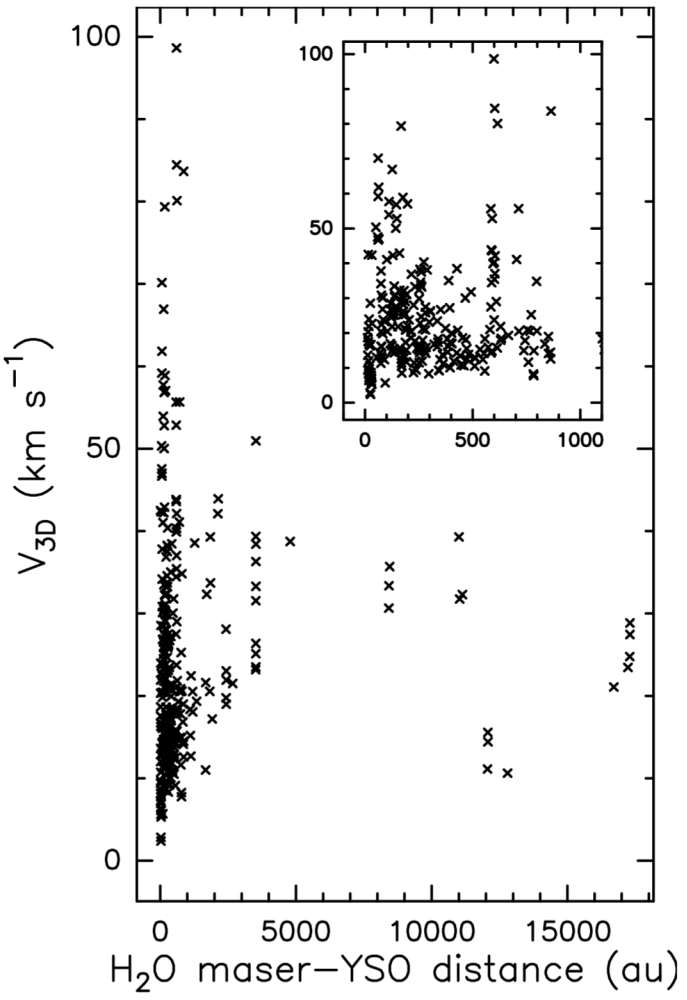

Fig. 6. Amplitude of the 3D velocities of the H_2O masers vs. the distance from the YSO, cumulating all the POETS targets. The inset in the upper right corner shows an enlargement of the main plot for the distance range 0–1100 au.

for the shocks a factor of 3–10 smaller than that of the jet, in agreement with our measurements for the faster subset of water masers. Thus, we propose that the water masers showing higher velocities, that is, ≥30 km s^{-1}, or larger separation, at several 1000 au, from the YSO originate in J shocks owing to the interaction of the protostellar jet with the surrounding material.

Figure 6 presents the distribution of the 3D-velocity amplitude of the water masers versus the distance from the YSO. In particular, the plot in the inset shows that the large majority of the masers within 1000 au have speeds ≤30 km s^{-1}, and, following our interpretation, it should originate in internal C shocks of the YSOs DWs. Considering, instead, the near, ≤1000 au, fastest, ≥30 km s^{-1}, masers, we note that a significant fraction of them are found within 200 au from the YSO. The plot of Fig. 6 cumulates all the POETS targets, covering a large range in bolometric luminosities, 10^2–10^5 $L_\odot$, and YSO masses, 5–30 $M_\odot$. A corresponding large variation in the sizes of the kinematic structures (i.e., disks, DWs and jets) surrounding the YSOs is also expected. Then, the plot region ≤200 au and ≥30 km s^{-1} could correspond to water masers associated with the roots of the jets in lower-mass YSOs. Inspecting the main plot of Fig. 6, it is also remarkable that the minimum water maser velocity increases regularly with the distance from the YSO up to, at least, 4000–5000 au. Following our discussion, at separations of 1000–10000 au, water masers should mainly arise in J shocks excited in the jet-ambient interaction, and, on the basis of Eq. (2), a plausible interpretation is that the shock (and maser) velocities increase because the jet is continuously accelerated at this range of distances (Pudritz et al. 2007; Ramsey & Clarke 2019).

4. Conclusions

This paper presents a statistical analysis of the kinematic properties at mas resolution of a large sample of 994 H_2O masers, associated with 36 distinct YSOs. To our knowledge, this is the first VLBI survey of the 22 GHz H_2O masers, including a sizable number of sources and based on maser positions and 3D velocities determined with an accuracy of a few mas and a few km s^{-1}, respectively. The main results can be summarized as follows:

1. The 22 GHz water masers are a reliable proxy for the position of the YSOs: 84% of them are found within 1000 au from the YSO, and 45% within 200 au.
2. The distribution of maser luminosity is strongly peaked towards low values, indicating that about half of the maser population, with intensities ≤100 mJy beam^{-1}, remains undetected.
3. The PA of the water maser PMs provides a statistically-significant estimate for the PA of the YSO jet: 55% of the maser PMs are directed on the sky within an angle of 30° from the jet axis.
4. The 3D maser velocities have small (≤35°) inclinations with the plane of the sky and amplitudes mainly in the range of 10–30 km s^{-1}.

Regarding point 2, future sensitive interferometers (e.g., ngVLA) will serve as the appropriate instruments for studying the weaker, albeit conspicuous, water maser population predicted in this work. Concerning points 3 and 4, we stress that for the first time we are providing a statistic for the amplitude and directions of 3D velocities for the 22 GHz water masers. We find that water masers moving almost parallel to the plane of the sky are preferentially detected. This result fully supports the shock models for the origin of the water masers, where a long velocity-coherent, amplification path along the LOS is predicted for planar shocks with propagation direction close to the plane of the sky. In Paper III, which focused on the maser kinematics, we proposed that the water masers near the YSOs trace the different regions of a DW, from the fast and collimated jet portion to the slower, wide-angle outer layers. Following this interpretation, we can now make a prediction on the nature of the maser shocks. While most of the water masers with lower speed, that is, ≤30 km s^{-1}, should be excited in weak, internal C shocks occurring in the slower regions of the DWs, most of the masers at higher velocity, that is, ≥30 km s^{-1}, should originate in strong J shocks wherever the fast jets hit the ambient medium.

References

Anglada, G., Estalella, R., Pastor, J., Rodriguez, L. F., & Haschick, A. D. 1996, ApJ, 463, 205
Anglada, G., Rodríguez, L. F., & Carrasco-González, C. 2018, A&ARv, 26, 3
Beuther, H., Walsh, A., Schilke, P., et al. 2002, A&A, 390, 289
Beuther, H., Linz, H., & Henning, T. 2013, A&A, 558, A81
Burns, R. A., Handa, T., Nagayama, T., Sunada, K., & Omodaka, T. 2016, MNRAS, 460, 283
Cheung, A. C., Rank, D. M., Townes, C. H., Thornton, D. D., & Welch, W. J. 1969, Nature, 221, 626
Elitzur, M., Hollenbach, D. J., & McKee, C. F. 1989, ApJ, 346, 983
Elitzur, M., Hollenbach, D. J., & McKee, C. F. 1992, ApJ, 394, 221

Felli, M., Brand, J., Cesaroni, R., et al. 2007, A&A, 476, 373
Furuya, R. S., Kitamura, Y., Wootten, H. A., Claussen, M. J., & Kawabe, R. 2001, ApJ, 559, L143
Goddi, C., & Moscadelli, L. 2006, A&A, 447, 577
Goddi, C., Moscadelli, L., Torrelles, J. M., Uscanga, L., & Cesaroni, R. 2006, A&A, 447, L9
Hollenbach, D., Elitzur, M., & McKee, C. F. 2013, ApJ, 773, 70
Hunter, T. R., Brogan, C. L., Bartkiewicz, A., et al. 2018, ASP Conf. Ser., 517, 321
Ilee, J. D., Cyganowski, C. J., Nazari, P., et al. 2016, MNRAS, 462, 4386
Johnston, K. G., Robitaille, T. P., Beuther, H., et al. 2015, ApJ, 813, L19
Kaufman, M. J., & Neufeld, D. A. 1996, ApJ, 456, 250
Kim, W.-J., Kim, K.-T., & Kim, K.-T. 2019, ApJS, 244, 2
Kölligan, A., & Kuiper, R. 2018, A&A, 620, A182
Masson, C. R., & Chernin, L. M. 1993, ApJ, 414, 230
Moscadelli, L., Cesaroni, R., & Rioja, M. J. 2005, A&A, 438, 889
Moscadelli, L., Sánchez-Monge, Á., Goddi, C., et al. 2016, A&A, 585, A71
Moscadelli, L., Sanna, A., Goddi, C., et al. 2019a, A&A, 631, A74
Moscadelli, L., Sanna, A., Cesaroni, R., et al. 2019b, A&A, 622, A206
Pudritz, R. E., & Banerjee, R. 2005, IAU Symp., 227, 163
Pudritz, R. E., Ouyed, R., Fendt, C., & Brandenburg, A. 2007, in Protostars and Planets V, eds. B. Reipurth, D. Jewitt, & K. Keil (Tuson: University of Arizona Press), 277
Ramsey, J. P., & Clarke, D. A. 2019, MNRAS, 484, 2364
Reid, M. J., Menten, K. M., Brunthaler, A., et al. 2014, ApJ, 783, 130
Reid, M. J., Menten, K. M., Brunthaler, A., et al. 2019, ApJ, 885, 131
Rosero, V., Hofner, P., Kurtz, S., et al. 2019, ApJ, 880, 99
Sanna, A., Reid, M. J., Carrasco-González, C., et al. 2012, ApJ, 745, 191
Sanna, A., Moscadelli, L., Goddi, C., Krishnan, V., & Massi, F. 2018, A&A, 619, A107
Sanna, A., Moscadelli, L., Goddi, C., et al. 2019a, A&A, 623, L3
Sanna, A., Kölligan, A., Moscadelli, L., et al. 2019b, A&A, 623, A77
Titmarsh, A. M., Ellingsen, S. P., Breen, S. L., Caswell, J. L., & Voronkov, M. A. 2016, MNRAS, 459, 157
Torrelles, J. M., Patel, N. A., Anglada, G., et al. 2003, ApJ, 598, L115
Urquhart, J. S., Morgan, L. K., Figura, C. C., et al. 2011, MNRAS, 418, 1689
Walsh, A. J., Breen, S. L., Britton, T., et al. 2011, MNRAS, 416, 1764
Walsh, A. J., Purcell, C. R., Longmore, S. N., et al. 2014, MNRAS, 442, 2240

Appendix A: Table

Table A.1. Water masers and radio continuum.

Source	d	L_{bol}	YSO continuum [a]		N_{mas}	Maximum radius
			RA (J2000)	Dec (J2000)		
	(kpc)	($L_\odot$)	(h m s)	(° ′ ″)		(au)
G005.88−0.39	2.99 ± 0.18	5.8×10^4	18 00 30.440	−24 04 00.90	26	16 708
G009.99−0.03 [b]	*5.0*	*1.2×10^4*	18 07 50.117	−20 18 56.49	16	801
G011.92−0.61	3.37 ± 0.35	1.2×10^4	18 13 58.112	−18 54 20.19	27	776
G012.43−1.12 [b]	*3.7*	*4.2×10^4*	18 16 52.161	−18 41 43.94	3	227
G012.68−0.18	2.40 ± 0.18	5.7×10^3	18 13 54.750	−18 01 46.58	21	630
G012.90−0.24	2.45 ± 0.15	8.6×10^2	18 14 34.428	−17 51 51.80	2	130
G014.64−0.58	1.83 ± 0.07	1.1×10^3	18 19 15.546	−16 29 45.83	5	185
G016.58−0.05	3.58 ± 0.30	1.3×10^4	18 21 09.125	−14 31 48.65	35	2179
G026.42+1.69 [b]	*3.1*	*9.0×10^3*	18 33 30.508	−05 01 01.95	7	275
G031.58+0.08	4.90 ± 0.72	2.0×10^4	18 48 41.613	−01 09 57.70	11	11 484
G035.02+0.35	2.33 ± 0.22	1.0×10^4	18 54 00.649	+02 01 19.41	27	621
G049.19−0.34	5.29 ± 0.20	6.0×10^3	19 22 57.771	+14 16 09.91	11	254
G074.04−1.71	1.59 ± 0.05	*3.7×10^2*	20 25 07.117	+34 49 57.53	29	586
G075.76+0.34	3.51 ± 0.28	1.4×10^4	20 21 41.093	+37 25 29.19	19	453
G075.78+0.34	3.72 ± 0.43	1.1×10^4	20 21 44.013	+37 26 37.51	61	2439
G076.38−0.62	1.30 ± 0.09	*1.4×10^4*	20 27 25.477	+37 22 48.42	50	115
G079.88+1.18	1.61 ± 0.07	8.6×10^2	20 30 29.145	+41 15 53.54	6	178
G090.21+2.32	0.67 ± 0.02	2.7×10^1	21 02 22.703	+50 03 08.27	15	38
G092.69+3.08	1.63 ± 0.05	(*4.7×10^3*)	21 09 21.714	+52 22 37.02	50	275
G097.53+3.18–M	7.52 ± 0.96	(*8.8×10^4*)	21 32 12.451	+55 53 49.76	82	1923
G100.38−3.58	3.44 ± 0.10	*8.5×10^3*	22 16 10.365	+52 21 34.14	49	755
G105.42+9.88 [c] 3A	0.89 ± 0.05	(*5.8×10^2*)	21 43 06.474	+66 06 54.98	2	15
G105.42+9.88 [c] 3B	0.89 ± 0.05	(*5.8×10^2*)	21 43 06.460	+66 06 55.18	72	23
G108.20+0.59	4.37 ± 0.53	2.1×10^3	22 49 31.465	+59 55 41.86	39	452
G111.24−1.24	3.47 ± 0.53	*1.0×10^4*	23 17 20.891	+59 28 47.60	21	3575
G111.25−0.77	3.40 ± 0.18	*5.0×10^3*	23 16 10.331	+59 55 28.63	57	1268
G160.14+3.16	4.10 ± 0.10	*8.4×10^3*	05 01 39.914	+47 07 21.58	5	17 304
G168.06+0.82	7.69 ± 2.37	1.6×10^4	05 17 13.743	+39 22 19.85	15	1849
G176.52+0.20	0.96 ± 0.02	1.5×10^2	05 37 52.136	+32 00 03.93	71	177
G182.68−3.27	6.71 ± 0.50	*8.6×10^2*	05 39 28.419	+24 56 32.16	3	347
G183.72−3.66	1.75 ± 0.04	*9.7×10^2*	05 40 24.230	+23 50 54.68	22	117
G229.57+0.15 [d] 1	4.52 ± 0.29	2.2×10^3	07 23 01.845	−14 41 32.79	2	161
G229.57+0.15 [d] 2	4.52 ± 0.29	2.2×10^3	07 23 01.804	−14 41 32.94	26	389
G236.82+1.98	3.36 ± 0.20	*2.3×10^3*	07 44 28.239	−20 08 30.19	44	560
G240.32+0.07	4.72 ± 0.47	8.3×10^3	07 44 52.040	−24 07 42.21	10	8473
G359.97−0.46 [b]	*4.0*	*5.7×10^4*	17 47 20.188	−29 11 59.04	4	975
AFGL 5142	2.14 ± 0.05	5.0×10^3	05 30 48.018	+33 47 54.54	23	469
IRAS 20126+4104	1.64 ± 0.05	1.3×10^4	20 14 26.054	+41 13 32.49	26	865

Notes. Column 1 reports the name of the POETS targets: the two sources in italic characters have been observed prior of the POETS survey; Cols. 2 and 3 give the trigonometric parallax distance from BeSSeL (available for all but four sources, for which the kinematic distance is reported) and the evaluated bolometric luminosity, respectively: kinematic distances and more uncertain luminosities are given in italic characters, and values which might be severe upper limits are enclosed within brackets; Cols. 4 and 5 give the RA and Dec coordinates, respectively, of the YSO, pinpointed by JVLA, high-angular resolution, radio continuum observations; Cols. 6 and 7 list the number of detected maser cloudlets and the maximum maser separation from the YSO, respectively. [a]In a few cases where the continuum emission shows two nearby peaks, we choose the peak closer to most of the water masers. In three objects, G005.88−0.39, IRAS 20126+4104, and AFGL 5142, previously studied at subarcsecond resolution with millimeter and near-infrared interferometers, we have used the position of the YSO identified through continuum or molecular line emissions. [b]In this target, the water maser emission has faded away over the VLBI observing epochs, and nor trigonometric parallax distance neither reliable maser proper motions have been measured. [c]In this target, the water maser emission comes from two nearby YSOs, resolved through subarcsecond VLA observations, named VLA 3A and VLA 3B. [d]In this target, the water maser emission comes from two nearby YSOs, resolved through subarcsecond VLA observations, named VLA-1 and VLA-2.